Supporting Information

Highly Efficient Surface-Emitting Light Source Enabled by Silicon Nitride Photonic Crystal Cavities Coupled with Perovskite Quantum Dots

*Rongzi Wang[1‡], Ying Su[1‡], Na Jia[1‡], Hongji Fan[1], Chengxiang Qi[1], and Tun Cao[1,2‡]**

[1]School of Optoelectronic Engineering and Instrumentation Science, Dalian University of Technology, Dalian, Liaoning 116024, China
[2]Suzhou Laboratory, Suzhou, 215000, Jiangsu, China
[‡]These authors contributed equally
*Corresponding author: caotun1806@dlut.edu.cn

1. The complex refractive index of PMMA film and silicon nitride layer

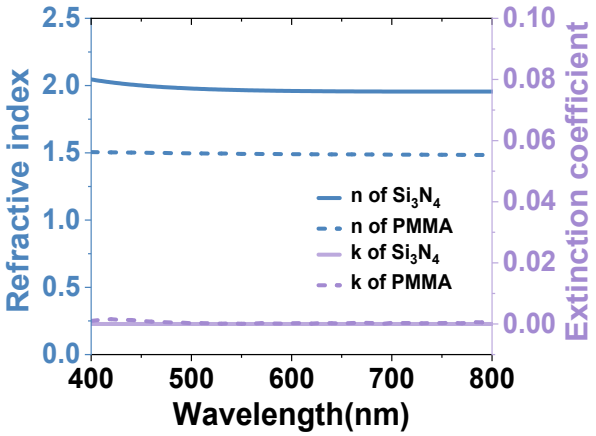

Figure S1. The refractive index and extinction coefficient of PMMA film and Si_3N_4 layer.

The optical properties of the materials were characterized using a variable angle ellipsometer (J. A. Woollam, V-VASE), as illustrated in Figure S1. The complex refractive index was measured over a wavelength range of 400–800 nm, with a spectral resolution of 5 nm. In the visible light spectrum, the extinction coefficients of both PMMA and Si_3N_4 are negligible. The refractive index of PMMA at approximately 510 nm is around 1.5, which is nearly identical to that of SiO_2 (~1.46). This suggests that the PMMA/Si_3N_4/SiO_2 three-layer film platform exhibits an almost symmetric refractive index profile in the vertical direction.

2. The Optimizing of the Si_3N_4 PhC heterostructure cavity

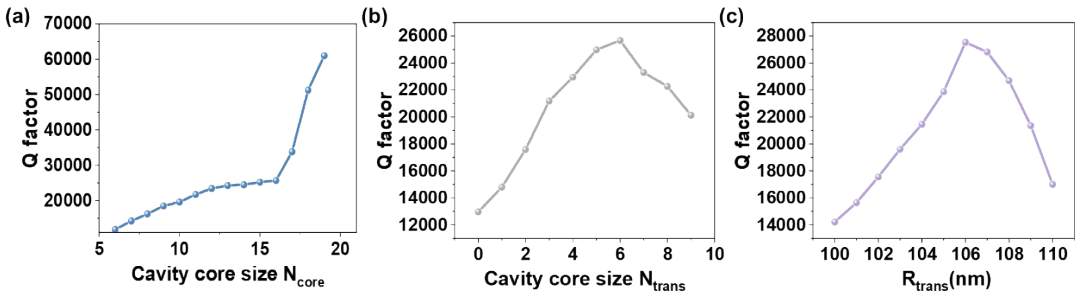

Figure S2. Simulated the Q factor depending on a) N_{core}, b) N_{trans} and c) R_{trans}.

We simulated a series of heterostructure photonic crystals (PhCs) with varying size parameters to investigate the effect of size on the quality factor (Q factor) of the fundamental cavity mode. The results are summarized in Figure S2. Based on previous studies,[S1] which indicated that when the number of clad layers (N_{clad}) exceeds 25, the Q factor does not significantly increase, we set N_{clad} to 30 in the present work. This behavior is attributed to the fact that the dominant leakage channels are already effectively blocked once the cladding region exceeds a sufficient number of periods, and additional periods contribute negligibly to confinement. In Figure S2a, the cavity under consideration has varying values of N_{core}, with fixed N_{trans} = 6 and N_{clad} = 30. It is observed that as N_{core} increases, the Q factor increases monotonically. This suggests that as N_{core} approaches infinity, the mode will converge to a true bound state in the continuum (BIC) with an infinite Q factor. Since the experimentally measured Q factor is limited by the instrumental resolution and excessively high theoretical values cannot be accurately validated, we therefore selected N_{core} = 16 in this study. In Figure S2b, we present the Q factor as a function of N_{trans} while keeping N_{core} constant at 16 and N_{clad} constant at 30. The Q factor is found to be maximized when N_{trans} = 6. As shown in Figure 1c, the mode gap appears between the bands of the core and cladding regions. When the lattice period is fixed, the values of R_{core} and R_{clad} primarily determine the resonance wavelength of the cavity, which should be designed to match the photoluminescence spectrum of the perovskite quantum dots after spin-coating with PMMA. Meanwhile, the transition region serves as an intermediate zone, implying the

existence of an optimal R_{trans} value that maximizes the Q factor. Therefore, these parameters are optimized by balancing mode confinement, fabrication feasibility, and compatibility with the desired resonance wavelength. As shown in Figure S2c, when N_{core} = 16, N_{trans} = 6, and N_{clad} = 30 are fixed, the Q factor reaches its maximum when R_{trans} = 106 nm.

It is worth noting that in the FDTD simulation of the designed PhC cavity, the electromagnetic field does not fully decay within the limited simulation time. As a result, the resonance spectrum shown in **Figure** 2 provides an accurate representation of the resonance wavelengths and relative intensities, but it does not allow for direct extraction of the Q factor. To determine the Q value, further analysis of the temporal decay of the electromagnetic signal is required, involving the extraction of the decay envelope and subsequent calculation based on the resonant frequency.

The Q factor of a resonant cavity is defined as:

$$Q = \frac{\lambda}{FWHM} \tag{1}$$

where λ is the resonant wavelength and FWHM is the full width at half maximum. The time-domain signal of the resonance can be expressed as:

$$E(t) = e^{-r(\alpha - i\omega_r)}u(t) \tag{2}$$

where α is the decay constant and ω_r is the resonant angular frequency. Taking the Fourier transform of E(t), we get:

$$|E(\omega)|^2 = \frac{1}{\alpha^2 + (\omega - \omega_r)^2} \tag{3}$$

This indicates that the maximum occurs at $\omega = \omega_r$, with a peak value of $1/\alpha^2$. The half-maximum values occur at $\omega = \omega_r \pm \alpha$ leading to a full width at half maximum of FWHM = 2α. Substituting into equation (1), we obtain the following:

$$\alpha = \frac{\omega_r}{2Q} \tag{4}$$

To relate the decay slope *m* of the time-domain signal to the Q factor, we take the

logarithm of equation (2), yielding a linear relation:

$$\log_{10}(|E(t)|) = \frac{-\omega_r t}{2Q}\log_{10}(e) = mt \tag{5}$$

Hence, the Q-factor can be expressed as:

$$Q = \frac{-\omega_r \log_{10}(e)}{2m} \tag{6}$$

3. Simulated electric field distribution

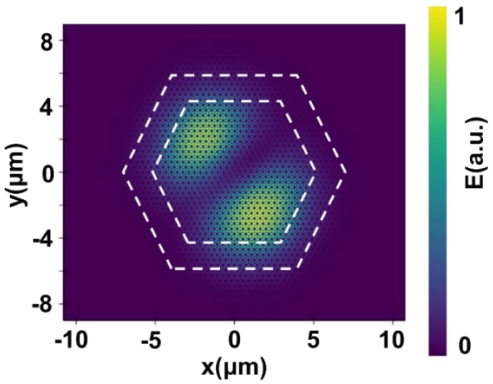

Figure S3. Simulated electric field distribution of the second-order cavity mode on the cavity structure (N_{core} =16, N_{trans} =6, and Nclad =30). The dashed lines indicate the separation between regions.

4. The fabrication of Si_3N_4 PhC heterostructure cavity air holes array template

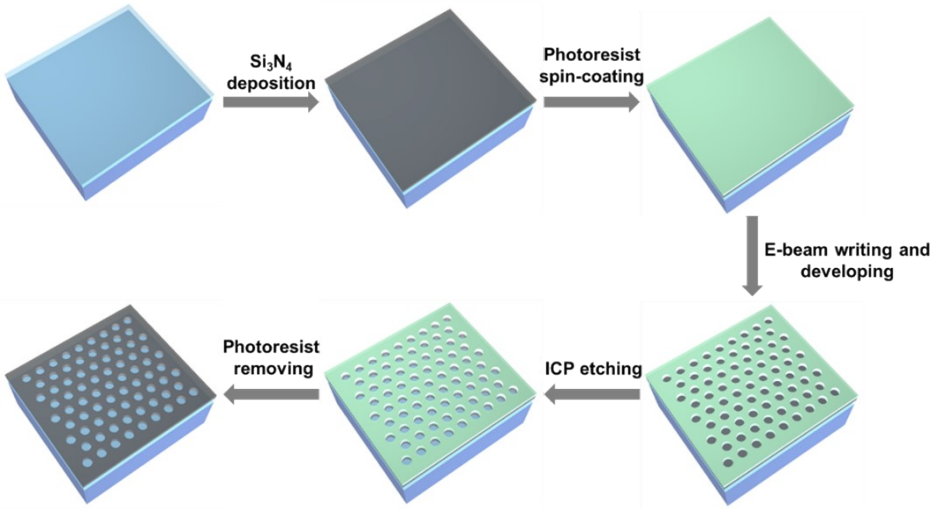

Figure S4. Fabrication process of Si_3N_4 air holes array based on electron beam lithography (EBL).

Figure S4 offers a more intuitive depiction of the fabrication process flow for the PhC heterostructure cavity, with detailed parameters provided in the Methods section of the main text. The PhC cavities were fabricated on a 102 nm thick Si_3N_4 membrane, which was grown via plasma-enhanced chemical vapor deposition (PECVD) using an OXFORD PlasmaPro 100 system, and supported on a 2 μm thick silicon dioxide layer. A 250 nm layer of ZEP-520 electron beam resist was spin-coated (3000 rpm for 60 seconds) onto the 1×1 cm^2 Si_3N_4 membrane, followed by baking at 150°C for 3 minutes. The pattern was defined in the resist using electron-beam lithography (JEOL JBX-9500FS, 100 kV), after which it was transferred into the Si_3N_4 membrane through reactive ion etching (RIE) with an $SF_6/CHF_3/O_2$ gas mixture, utilizing an OXFORD PlasmaPro 100 RIE system. The residual resist was then removed using a gentle oxygen plasma RIE process. Finally, the entire substrate was thoroughly cleaned with deionized water.

5. Further details on optical characterization

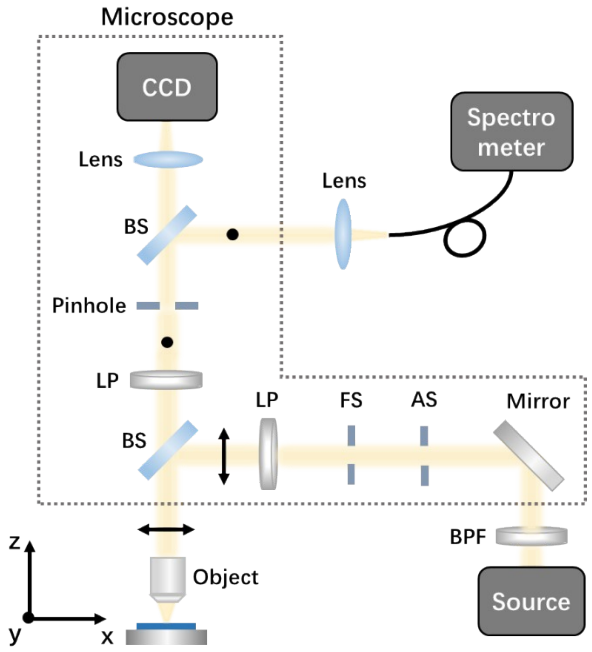

Figure S5. Schematic of the photonic crystal heterostructure cavity test setup.

The measurement setup is based on a confocal microscope system (Olympus BX53M), as delineated by the gray dashed region in Figure S5. The field stop (FS) and aperture stop (AS) of the microscope define the spatial coherence and illumination geometry, respectively. Collimated broadband white light is first spectrally filtered using a bandpass filter (BPF) to produce a light source with the desired spectral bandwidth. This filtered beam then passes through a linear polarizer (LP) to generate horizontally polarized illumination, which is focused onto the sample surface using a 100× objective lens with a numerical aperture (NA) of 0.8. The reflected light from the sample is subsequently analyzed using a second polarizer (analyzer) oriented orthogonally to the incident polarization, effectively suppressing non-resonant reflection components. To further enhance the signal-to-noise ratio, the reflected beam is directed through a spatial pinhole positioned at the imaging plane of the microscope. This pinhole restricts detection to a localized region (~20 μm in diameter) on the sample surface by limiting the light collected through the objective, thereby reducing background scattering and surface-reflection noise and enhancing the precision of resonance peak detection. The pinhole has a physical diameter of 2 mm. Finally, the collected optical signal is split and directed to both a CCD camera and a grating spectrometer (Horiba iHR 320), offering a spectral resolution of approximately 0.019 nm.

6. Enlarged SEM images of the air hole structures in the three regions

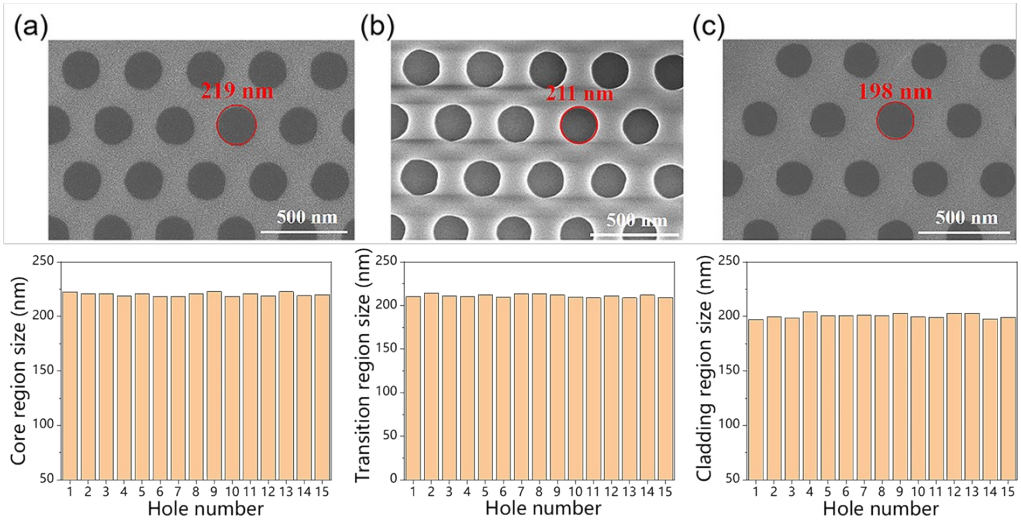

Figure S6. Enlarged SEM images of the fabricated photonic crystal structure in the (a) core region, (b) transition region, and (c) cladding region, together with the corresponding air-hole diameter distributions for each region.

Figure S6a-c present high-magnification SEM images of the local unit-cell structures in the core, transition, and cladding regions, respectively, with a scale bar of 500 nm. In Figure S6a, a representative air hole in the core region (highlighted by a red circle) has a measured diameter of 219 nm; in Figure S6b, the marked air hole in the transition region measures 211 nm; and in Figure S6c, the cladding-region air hole is 198 nm in diameter. The air-hole diameters in all three regions exhibit narrow distributions (standard deviation ~2.5 nm) with slight deviations from ideal circularity (Figure S6), which can accumulate across the cavity and explain the observed deviations from the ideal simulated model. The gradual variation of air-hole sizes across these regions is consistent with the designed gradient distribution, which facilitates effective mode coupling and leakage control. However, slight reductions in air-hole diameters and minor shape distortions were introduced during the EBL and RIE processes.

7. Effect of PMMA penetration depth

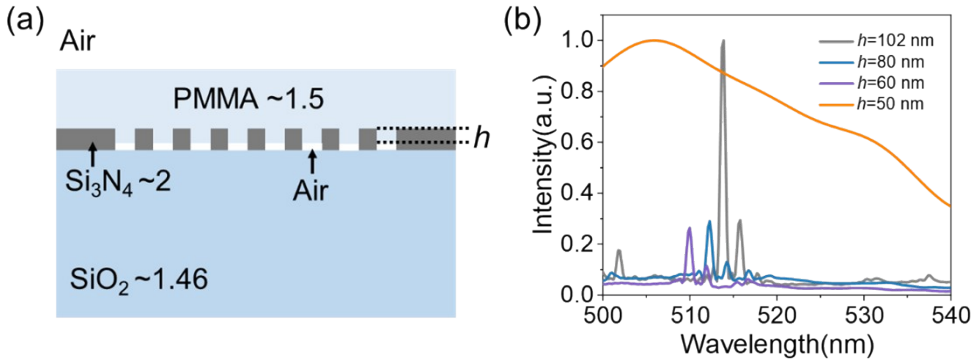

Figure S7. (a) Schematic illustration of the simulated structure with the different degrees of PMMA infiltration. (b) The simulated scattering spectra of the PhC cavity with h = 102 nm, 80 nm, 60 nm, and 50 nm.

8. Optical properties of $CsPbBr_3$ QDs mixed in PMMA

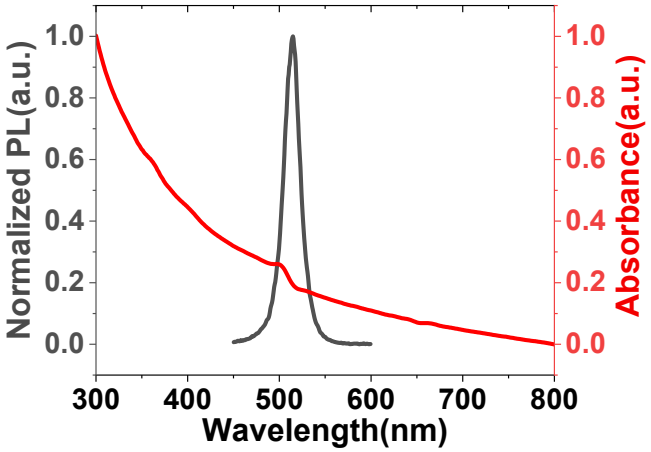

Figure S8. Normalized absorption and photoluminescence (PL) spectrum of $CsPbBr_3$ QDs mixed in PMMA.

9. Time-resolved Photoluminescence spectra of $CsPbBr_3$ QDs

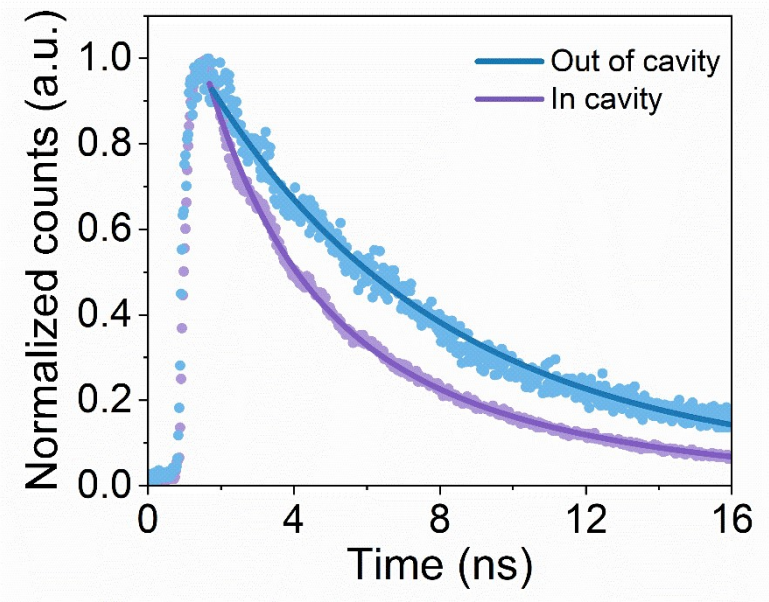

Figure S9. Normalized time-resolved PL from $CsPbBr_3$ QDs outside the PhC cavity (blue) and within the PhC cavity (purple). Discrete data points represent the raw experimental measurements.

Figure S9 presents the normalized time-resolved PL spectra of $CsPbBr_3$ QDs both within and outside the PhC cavity regime. For QDs located outside the cavity, which are embedded in the same microenvironment and exhibit identical decay pathways, the PL decay behavior conforms to a biexponential function:

$$I(t) = I_0 + A_1 e^{-\frac{t}{\tau_1}} + A_2 e^{-\frac{t}{\tau_2}} \tag{7}$$

where I_0 denotes the background intensity, τ_1 and τ_2 denote the lifetimes of the fast and slow decay components, and A_1 and A_2 are their respective amplitudes. The fit yields $\tau_1 = 2.5$ ns (A_1 of 0.35), and $\tau_2 = 6.8$ ns (A_2 of 0.6). The slow component τ_2 reflects the intrinsic spontaneous emission of uncoupled QDs in the absence of the cavity, and its value is consistent with previously reported lifetimes for $CsPbBr_3$ QDs.

In contrast, QDs within the PhC cavity reside in two distinct microenvironments: uncoupled QDs and QDs coupled to the cavity mode. The coupled population exhibits a fast decay component τ_2 = 2.13 ns (A_2 of 0.49), corresponding to enhanced spontaneous emission due to the cavity coupling. The slow component $\tau_1 = 6.71$ ns (A_1

of 0.52), which represents the uncoupled QDs. Here, $\tau_{2,out}$ and $\tau_{2,in}$ denote the slow component of uncoupled QDs outside the cavity and the fast component of coupled QDs within the cavity, respectively. Focusing on the coupled population, the spontaneous emission enhancement factor is calculated as $\tau_{2,out}$ / $\tau_{2,in}$≈6.8 ns /2.13 ns≈3.2, confirming the cavity-induced acceleration of the coupled QDs.

10. Effect of quantum dot distribution

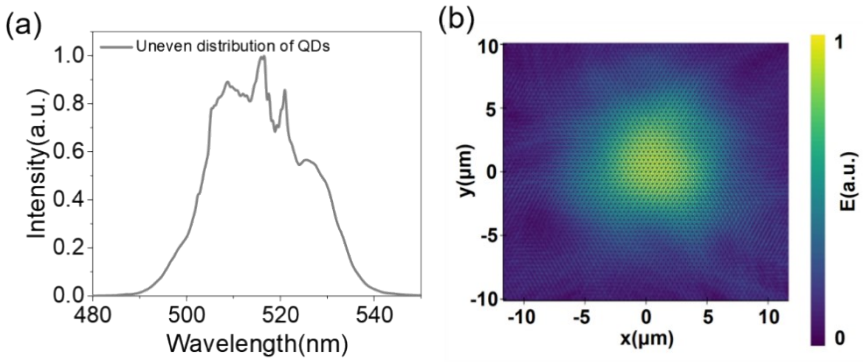

Figure S10. (a) Resonance spectrum of the PhC cavity with an uneven distribution of QDs, showing a broadened profile due to disrupted mode confinement. (b) Simulated electric field distribution corresponding to the PhC cavity with an inhomogeneous QD distribution, illustrating distortion of the cavity mode and degradation of optical confinement.

11. A PL-vs-time-in-air test under continuous illumination of QDs

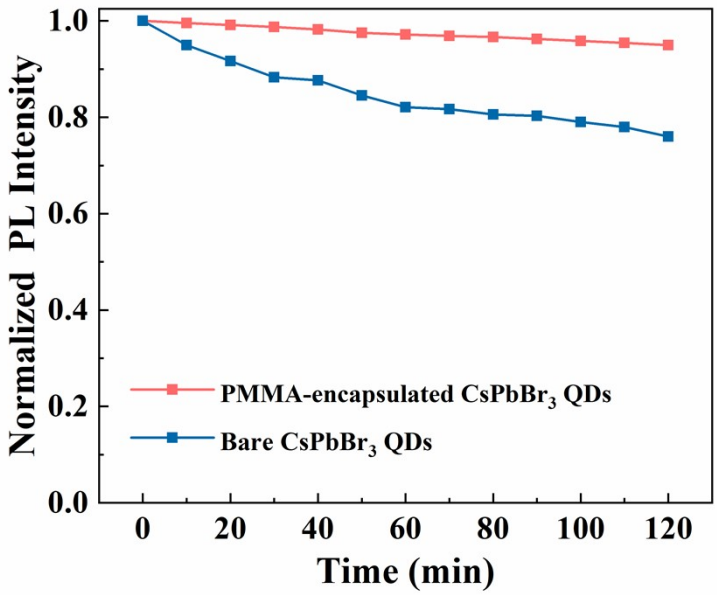

Figure S11. Time-dependent normalized photoluminescence (PL) intensity of bare and PMMA-encapsulated $CsPbBr_3$ QD films under continuous 405 nm laser excitation (0.5 W cm^{-2}) in ambient air (T ≈ 25 °C, RH ≈ 50%).

PL stability of $CsPbBr_3$ QD films was evaluated under continuous 405 nm laser illumination (0.5 W cm^{-2}) in ambient air (T ≈ 25 °C, RH ≈ 50%). Figure S11 shows the time-dependent normalized PL intensity for both bare and PMMA-encapsulated films. After 120 min of continuous illumination, the PMMA-encapsulated film retained over 96% of its initial PL intensity, while the bare film decreased to approximately 76%. These results indicate that PMMA encapsulation significantly improves the stability of $CsPbBr_3$ QDs.

REFERENCES

[S1] Ge, X.; Minkov, M.; Fan, S.; Li, X.; Zhou, W. Low index contrast heterostructure photonic crystal cavities with high quality factors and vertical radiation coupling. *Applied Physics Letters* **2018**, *112* (14). DOI：10.1063/1.5026433.